arXiv:1707.05346v1 [physics.plasm-ph] 17 Jul 2017

Electrostatic and whistler instabilities excited by an electron beam

Xin An,[1, a)] Jacob Bortnik,[1] Bart Van Compernolle,[2] Viktor Decyk,[2] and Richard Thorne[1]

[1)] *Department of atmospheric and oceanic sciences, University of California, Los Angeles*

[2)] *Department of physics and astronomy, University of California, Los Angeles*

(Dated: 14 December 2021)

The electron beam-plasma system is ubiquitous in the space plasma environment. Here, using a Darwin particle-in-cell method, the excitation of electrostatic and whistler instabilities by a gyrating electron beam is studied in support of recent laboratory experiments. It is assumed that the total plasma frequency ω_{pe} is larger than the electron cyclotron frequency Ω_e. The fast-growing electrostatic beam-mode waves saturate in a few plasma oscillations by slowing down and relaxing the electron beam parallel to the background magnetic field. Upon their saturation, the finite amplitude electrostatic beam-mode waves can resonate with the tail of the background thermal electrons and accelerate them to the beam parallel velocity. The slower-growing whistler waves are excited in primarily two resonance modes: (a) through Landau resonance due to the inverted slope of the beam electrons in the parallel velocity; (b) through cyclotron resonance by scattering electrons to both lower pitch angles and smaller energies. It is demonstrated that, for a field-aligned beam, the whistler instability can be suppressed by the electrostatic instability due to a faster energy transfer rate between beam electrons and the electrostatic waves. Such a competition of growth between whistler and electrostatic waves depends on the ratio of ω_{pe}/Ω_e. In terms of wave propagation, beam-generated electrostatic waves are confined to the beam region whereas beam-generated whistler waves transport energy away from the beam.

[a)] xinan@atmos.ucla.edu

I. INTRODUCTION

Energetic electron beams are ubiquitous throughout the solar system, such as the upstream from the interplanetary shock[1–3], the auroral ionosphere[4,5], solar flares[6], in the outflow region of magnetic reconnection[7,8] and possibly the Earth's outer radiation belt[9]. The electron beam provides a free energy source for generating various electrostatic and electromagnetic instabilities. For example, a finite amplitude single electrostatic wave can be excited by a small cold beam[10,11]. Whistler waves can also be excited by an electron beam in a number of space plasma settings[1,12–14]. Some electrostatic structures, such as double layers and electron holes, seems to be generated by current-carrying electron beams in the presence of density inhomogeneities[15]. Artificial electron beams have been injected into the Earth's ionosphere and magnetosphere to probe the space environment and to study the rich variety of waves in the beam-plasma interaction (see Ref. 16 and references therein). Extensive laboratory experiments in the past have been conducted to study the beam-generated whistler waves[17–19] and electrostatic waves[11]. Accordingly, many numerical experiments utilizing the particle-in-cell method were devoted to study the wave instabilities excited in the electron beam-plasma interaction[20–26].

A series of controlled laboratory experiments[27–29] were performed to study the excitation of whistler waves in the Large Plasma Device[30] at University of California, Los Angeles (UCLA). In the experiments, both electrostatic and whistler waves were excited by the injection of a gyrating electron beam into a cold plasma. It was demonstrated that the whistler mode waves were excited through a combination of cyclotron resonance, Landau resonance and anomalous cyclotron resonance[28]. A measurement of the electron distribution function is desired to study the self-consistent wave-particle interactions. But such a diagnostic of the electron distribution is not available at the present time. On the other hand, linear kinetic theory can predict the growth rate of electrostatic beam-mode and whistler waves for a given beam distribution. But the linear theory cannot resolve how the linearly unstable waves modify the electron distribution and therefore cannot resolve the saturation of the beam instability. Moreover, since both electrostatic beam-mode and whistler waves can extract energy from the inverted slope ($\partial f_b/\partial v_\parallel > 0$, f_b is the beam distribution function, $v_\parallel$ is the parallel velocity) of the electron beam through Landau resonance, the fast-growing

of electrostatic beam-mode waves can affect the slow-growing whistler instabilities via this inverted population. Here, using a self-consistent Darwin particle-in-cell method, we study the excitation of electrostatic and whistler waves in a beam-plasma system, the associated evolution of the electron distribution and the competing growth between electrostatic beam-mode and whistler waves.

II. COMPUTATIONAL SETUP

The Darwin particle-in-cell (PIC) model used in this study is based on a two-dimensional spectral code developed as part of the UCLA particle-in-cell (UPIC) framework[31,32]. The Darwin PIC model has been used previously to study the whistler anisotropy instability in the solar wind[33] and Earth's inner magnetosphere[34,35]. Compared to a conventional electromagnetic PIC method, the Darwin PIC method excludes the transverse component of the displacement current in Ampere's law and hence excludes retardation effects and light waves, but leaves the physics of whistler waves unaffected[36–38]. Thus the Darwin PIC model does not have the restriction on the time step set by Courant condition $\Delta t < \delta/c$. Here Δt is the time step used in the simulation, δ is the grid spacing and c is the speed of light. The grid spacing δ is required to resolve the Debye length to prevent numerical heating. Consequently, for a plasma having a background thermal component ($v_t/c = 0.01$) as in this study, the fully electromagnetic PIC method requires a very small time step ($\Delta t \lesssim 0.01\,\omega_{pe}^{-1}$) whereas the Darwin PIC method does not. Such an advantage greatly improves the computation efficiency.

A beam-plasma system with two dimensions of configuration space and three dimensions of velocity space is explored. The boundary conditions for both particles and fields are periodic in two spatial directions. The computational domain consists of $L_x = 4096$ grids in x direction and $L_y = 1024$ grids in y direction with a grid spacing of $0.02\,d_e$. Here $d_e = c/\omega_{pe}$ is the electron inertial length. ω_{pe} is the plasma frequency. Each cell contains 64 particles, which is sufficient to keep a low level of particle noise and converge the growth rate of instabilities. The time step is $0.1\,\omega_{pe}^{-1}$. The total simulation time is $500\,\omega_{pe}^{-1}$ to include both the linear and nonlinear stages of the instabilities. A uniform external magnetic field B_0 is applied in the x direction with a magnitude $\Omega_e/\omega_{pe} = 0.2$. In this study, the ions are

immobile and form a charge neutralizing background. A beam ring distribution is initialized in the system, which takes the form

$$f_b \propto e^{-\frac{\left(v_\parallel - V_{\parallel b}\right)^2}{2v_{tb\parallel}^2}} e^{-\frac{(v_\perp - V_{\perp b})^2}{2v_{tb\perp}^2}} \tag{1}$$

It has a streaming velocity $V_{\parallel b}/c = 0.0766$ parallel to the magnetic field and a velocity ring centered at $V_{\perp b}/c = 0.0766$ in the perpendicular direction, which corresponds to an electron beam of 3 keV in kinetic energy and 45 degree in pitch angle, which is typical in the experiment. The thermal spread of the beam is chosen as $v_{tb\parallel} = v_{tb\perp} = 0.001c$ so that the beam has a narrow "ring" in both parallel and perpendicular directions, mimicking that of the experiment. The beam density profile is localized in the y direction and uniform in the x direction, which takes the form

$$n_b(y) = \begin{cases} n_b, & \frac{3}{8}L_y < y < \frac{5}{8}L_y \\ 0, & \text{otherwise} \end{cases} \tag{2}$$

The beam width $L_y/4$ is about 13 times larger than the gyro-radius of the beam electrons, which is comparable to that in the experiment. In the beam region, the ratio of the beam density n_b to the total plasma density is $n_b/(n_b + n_0) = 1/8$, where n_0 is background plasma density in the beam region. Note that the ratio of beam density to total plasma density is about $0.001 \sim 0.005$ in the experiment, which is much lower than that in the simulation. Correspondingly, relevant quantities in the simulation, such as the linear growth rate and the saturation time of the waves, should be properly scaled to compare with that in the experiment. The background electrons form a return current that cancels the beam current in the parallel direction, i.e., $n_b V_{\parallel b} + n_0 V_{\parallel 0} = 0$. Here $V_{\parallel 0} = -V_{\parallel b}/7$ is the streaming velocity of background electrons in the beam region. Aside from this small streaming velocity in the beam region, the background electrons have an isotropic Maxwellian distribution with a thermal velocity of $0.01c$ (about 50 eV in thermal temperature). Outside the beam region, the density of background electrons is $n_b + n_0$ so that the total plasma density is uniform.

III. THE WAVE FIELD

A slice of wave field data, electric field δE_x and magnetic field δB_x, is taken along the x direction located at $y = L_y/2$ at every time step. The wave field δE_x and δB_x are Fourier-transformed to the space of ω - $k_\parallel$, where ω is the wave frequency and $k_\parallel$ is the parallel wave

number. The power spectral density of δE_x is shown in Figure 1a. Note that the magnetic power spectral density at the high frequencies around ω_{pe} is much weaker than the electric power spectral density. Thus the wave modes in Figure 1a are dominantly electrostatic. To identify the wave modes, the electrostatic dispersion relation is written as (assuming $k_\perp = 0$)

$$1 - \frac{\omega_{pe0}^2}{(\omega - k_\parallel V_{\parallel 0})^2}\left(1 + 3k_\parallel^2\lambda_D^2\right) - \frac{\omega_{pb}^2}{(\omega - k_\parallel V_{\parallel b})^2} = 0 \tag{3}$$

where λ_D is the Debye length of the thermal core electrons, ω_{pe0} is the plasma frequency of core electrons and ω_{pb} is the beam plasma frequency. Here the wave propagation is assumed to be parallel, i.e. $k_\perp = 0$, since the propagation angle is found to be within 20 degrees with respect to the background magnetic field. For a given $k_\parallel$, the dispersion relation is solved for a complex wave frequency ω. The real part of ω is shown for a spectrum of $k_\parallel$ as the white solid lines in Figure 1a. It is seen that the beam mode intersects with the Langmuir waves and modifies the topology of the dispersion relation of Langmuir waves. The electrostatic beam-mode waves has an enhanced power spectral density at $k_\parallel = 0.5 \sim 2\,\omega_{pe}/V_{\parallel b}$, which is consistent with the unstable range of the imaginary part of ω (not shown). Note that the intense electrostatic waves below ω_{pe} would not be present without an electron beam. The power spectral density of δB_x is shown in Figure 1b. The wave modes below Ω_e are whistler waves. The white solid line in Figure 1b represents the dispersion relation of a whistler wave propagating 55° with respect to the background magnetic field in a cold plasma. Whistler waves co-streaming with the beam ($k_\parallel > 0$) have a stronger power than the waves counter-streaming with the beam ($k_\parallel < 0$), indicating Landau resonance dominates over cyclotron resonance in the present settings.

Figure 2 shows the field pattern of electrostatic beam-mode waves and whistler waves in the post-saturation phase. In Figure 2a (Multimedia view), the longitudinal electric field, $\delta\mathbf{E}_L = -\nabla\phi$, along the x direction is displayed at $t = 300\,\omega_{pe}^{-1}$ after electrostatic beam-mode waves saturate. Here ϕ represents the electrostatic potential. This field pattern indicate the dominant nature of electrostatic waves at this time, since the electrostatic electric field energy of beam-mode waves is much larger than that of whistler waves. A Fourier analysis of the electrostatic wave field shows that substantial wave energy ranges in the parallel wave number k_x of 10 - 15 ω_{pe}/c, corresponding to 0.42 - 0.63 d_e in wavelength. The perpendicular wave number k_y of electrostatic beam-mode waves ranges between 0 - 4 ω_{pe}/c at the time of wave saturation, which is much smaller than the parallel wave number k_x. It is worthy

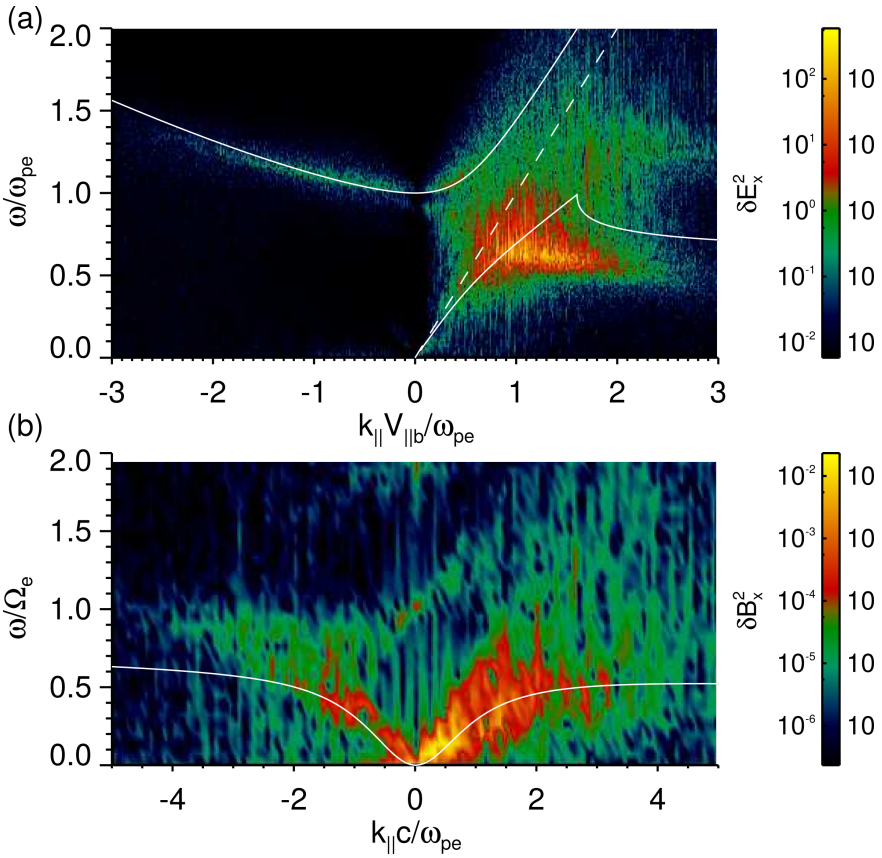


FIG. 1. (a) The power spectral density of δE_x. The solid white lines stand for the dispersion relation of electrostatic waves ($k_\perp = 0$) by solving equation (3). The dashed white line represents $\omega = k_\parallel V_{\parallel b}$. (b) The power spectral density of δB_x. The solid white line stands for the dispersion relation of a whistler wave propagating at 55° with respect to the background magnetic field in a cold plasma. Note that the parallel wave number $k_\parallel$ is normalized by $V_{\parallel b}/\omega_{pe}$ in panel (a) whereas it is normalized by c/ω_{pe} in panel (b), in order to better manifest the typical wave length of each wave.

to note that the excited electrostatic beam-mode waves only exist in the beam region (see the integral multimedia for an animation of the evolution of δE_{Lx}). In contrast, the excited whistler waves can propagate out of the beam region, as shown by the wave magnetic field δB_x in x direction in Figure 2b (Multimedia view). This snapshot is also taken at $t = 300\,\omega_{pe}^{-1}$ after whistler waves saturate. The beam-generated whistler waves have highly oblique wave fronts with $k_x = 1$ - $2\,\omega_{pe}/c$ and $k_y = 1$ - $4\,\omega_{pe}/c$ based on a Fourier analysis of the wave field, corresponding to a wavelength on the order of several electron inertial lengths. It is also noted that there are surface waves at the edge of the beam due to sharp boundaries of

the beam density profile (see equation (2)). To demonstrate that the energy is flowing out of the beam, the Poynting flux is integrated for all the wave modes along the x direction through the system. Note that the Poynting flux in the Darwin model (see Appendix B for details) differs from that in the electromagnetic model, i.e.,

$$\mathbf{S} = \frac{c}{4\pi}\left[(\mathbf{E}_L + \mathbf{E}_T) \times \mathbf{B} - \frac{1}{c}\mathbf{E}_T \frac{\partial \phi}{\partial t}\right] \tag{4}$$

Here $\mathbf{E}_L$ and $\mathbf{E}_T$ are the longitudinal and transverse components of electric field, respectively, satisfying $\nabla \times \mathbf{E}_L = 0$ and $\nabla \cdot \mathbf{E}_T = 0$. The y component of the integrated Poynting flux is shown in Figure 3. Inside the beam, the Poynting flux can be oriented in both the $+y$ and $-y$ directions, while outside the beam, it is directed only away from the beam indicating that the energy is flowing out of the beam. The region outside of the beam in Figure 3a is expanded and shown in Figure 3b. It is seen that the leading edge of the Poynting flux propagates away from the beam as time advances.

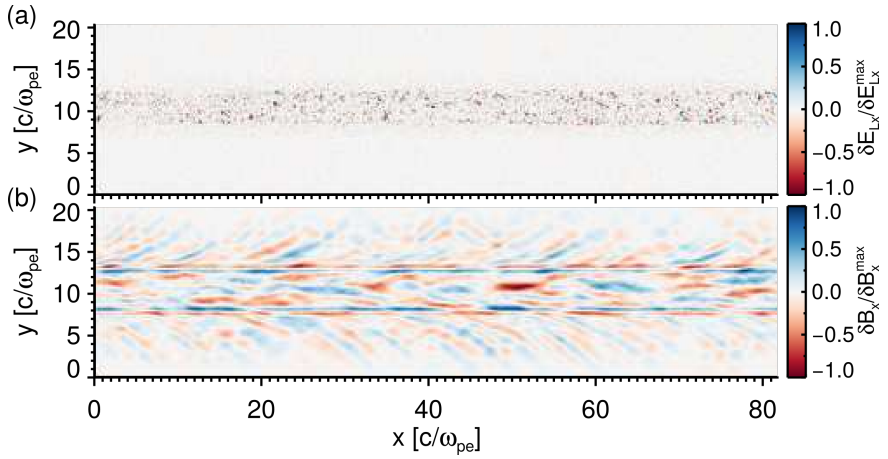


FIG. 2. (a) The field pattern of the longitudinal electric field along the x-direction at $t = 300\,\omega_{pe}^{-1}$. (Multimedia view) (b) The field pattern of the wave magnetic field along the x-direction at $t = 300\,\omega_{pe}^{-1}$. (Multimedia view)

IV. THE EXCITATION OF ELECTROSTATIC BEAM-MODE AND WHISTLER-MODE WAVES AND THE ASSOCIATED EVOLUTION OF THE ELECTRON DISTRIBUTION

We are now in a position to explore the excitation of electrostatic beam-mode and whistler waves and the associated evolution of the electron distribution. The time series data of the

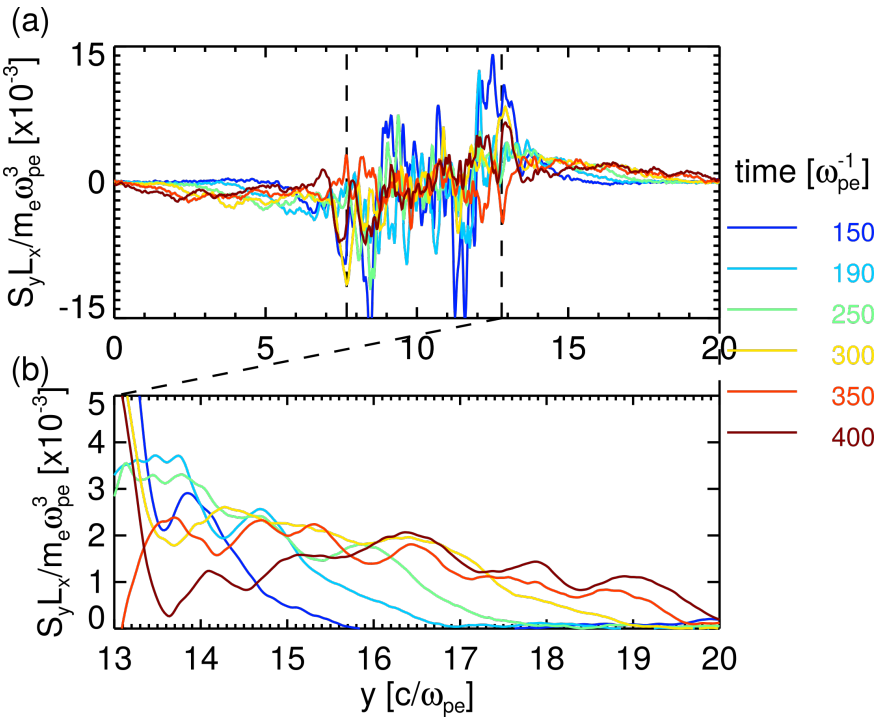


FIG. 3. (a) The y component of the integrated Poynting flux as a function y position. It is color coded by different time instants corresponding to the legend on the right. The beam region is between the two dashed lines. (b) An expanded display of the integrated Poynting flux for one side out of the beam indicating outflowing energy as a function of time.

electromagnetic fields is sampled at 32 locations centered in the x direction and equally spaced in the y direction inside the electron beam. A continuous wavelet transform which uses the Morlet wavelet function[39,40], is applied to the time series data of both the parallel electric field δE_x and the y component of the magnetic field δB_y. The results are shown in Figures 4a and 4b for δE_x and δB_y, respectively. Note that the power spectrum is averaged over 32 sampling locations to minimize its variance. Electrostatic beam-mode waves at ω/Ω_e = 3 - 5 dominate over other wave modes in the power spectrum of δE_x as shown in Figure 4a. They saturate in approximately five plasma oscillations (around $t = 30\,\omega_{pe}^{-1}$) and gradually damp out. Whistler waves show up prominently below the electron cyclotron frequency in the power spectrum of δB_y. Around $t = 100\,\omega_{pe}^{-1}$ ($\sim$ 3 cyclotron periods), whistler waves saturate with a primary peak at $\omega/\Omega_e = 0.6$ and a secondary peak at $\omega/\Omega_e = 0.25$. After saturation, the magnitude of these oblique whistler waves further decreases through Landau damping. To contrast the very different growth rates between

electrostatic beam-mode waves compared to whistler waves, two line cuts are taken from the wavelet spectral peaks, one at $\omega/\Omega_e = 3.5$ for electrostatic beam-mode waves and the other at $\omega/\Omega_e = 0.6$ for whistler waves. The results are shown in a linear-log plot in Figure 5. The magnitude of the linear growth rate corresponds to 1/2 of the slope in the linear part of the wave energy evolution. This linear growth rate is calculated to be $0.15\,\omega_{pe}$ for electrostatic beam-mode waves at $\omega/\Omega_e = 3.5$, and $0.015\,\omega_{pe}$ ($= 0.075\,\Omega_e$) for whistler waves at $\omega/\Omega_e = 0.6$. This calculation characterizes the rapidly growing electrostatic beam-mode waves and relatively slow-growing whistler waves. Note that before the electrostatic beam-mode wave saturates, whistler waves can also extract free energy from the inverted slope region (i.e., $\partial f_b/\partial v_\parallel > 0$) of the beam through Landau resonance, although the rate of such energy transfer is slower than that for the electrostatic beam-mode wave as shown in Figure 5. After the electrostatic beam-mode wave saturates, whistler waves can only be excited through cyclotron resonance since the free energy from $\partial f_b/\partial v_\parallel > 0$ has been exhausted by the electrostatic instability. Correspondingly, the electron distribution responds to the electrostatic and whistler instabilities on two different time scales. Figure 6 (Multimedia view) shows the electron distribution in velocity space, $v_\parallel$ - $v_\perp$ at four representative times. Note that the electrons are counted over the entire computation domain. To begin, the distribution is initialized with a population of core electrons and a separate population of beam ring electrons (Figure 6a). Shortly before the electrostatic beam-mode wave saturation at $t = 28\,\omega_{pe}^{-1}$, the beam electrons are trapped and relaxed by the electrostatic beam-mode waves in the parallel direction (Figure 6b). As the magnitude of the electrostatic beam-mode wave grows, the width of its resonant island broadens in $v_\parallel$ due to $\Delta v_\parallel \propto \sqrt{\delta E}$, where $\Delta v_\parallel$ is the width of the resonant island and δE is the electrostatic beam-mode wave amplitude. This large amplitude electrostatic wave becomes resonant with, and traps the tail of the core electrons and subsequently gets the tail of the core electrons accelerated to the beam energy level, as shown in Figure 6c at $t = 35\,\omega_{pe}^{-1}$. At a later time, the relaxed beam electrons are scattered along resonant diffusion surfaces to lower pitch angles and lose energy, through which whistler waves further gain energy and grow in magnitude. This is shown in Figure 6d taken at $t = 100\,\omega_{pe}^{-1}$ when the whistler waves saturate.

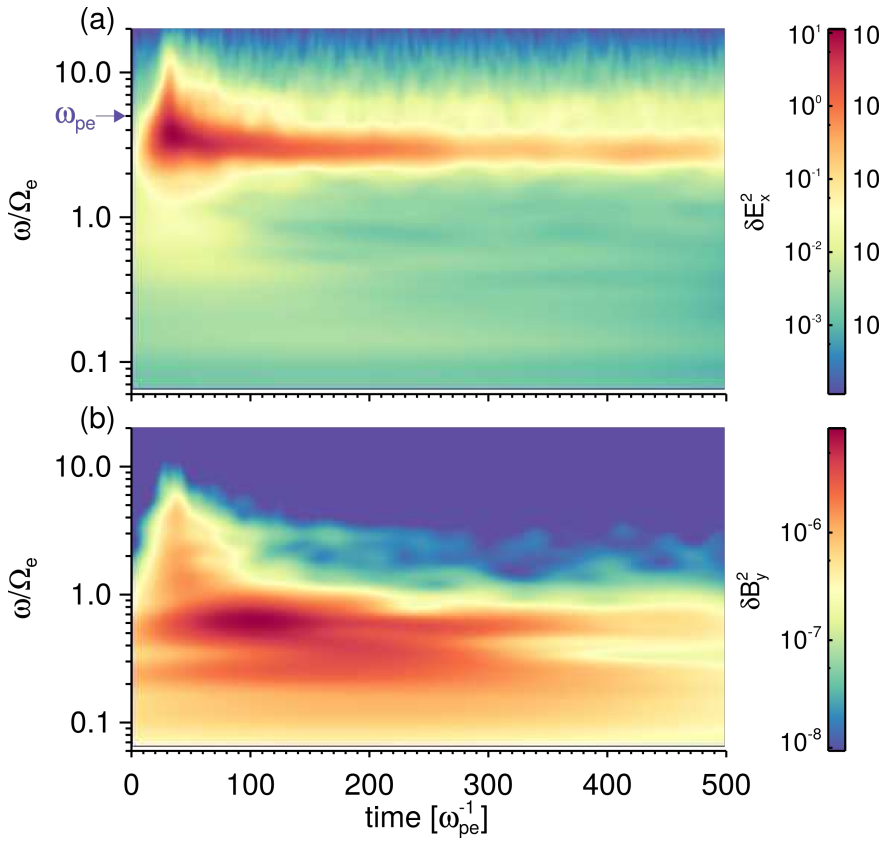


FIG. 4. (a) The power spectrum of δE_x evolving as a function of time. (b) The power spectrum of δB_y evolving as a function of time.

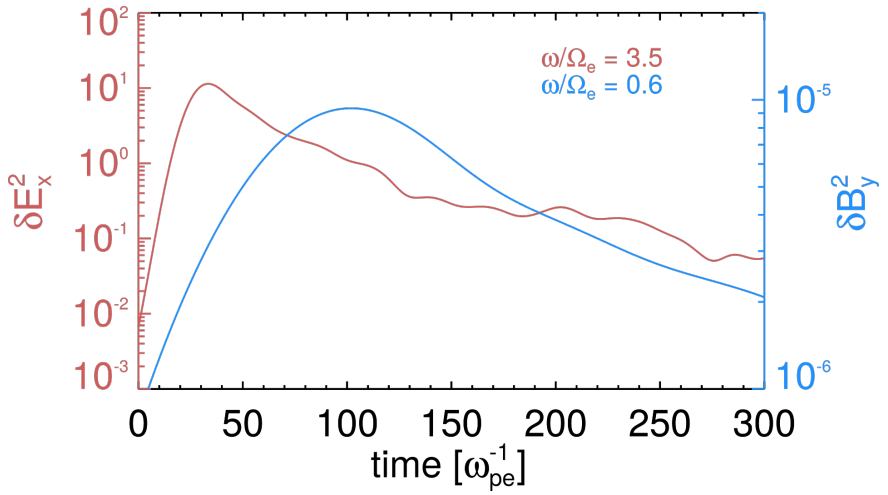


FIG. 5. The evolution of the power spectral density as a function of time. The power spectral density of δE_x at $\omega/\Omega_e = 3.5$ is shown as the red line with the y axis on the left. The power spectral density of δB_y at $\omega/\Omega_e = 0.6$ is shown as the blue line with the y axis on the right.

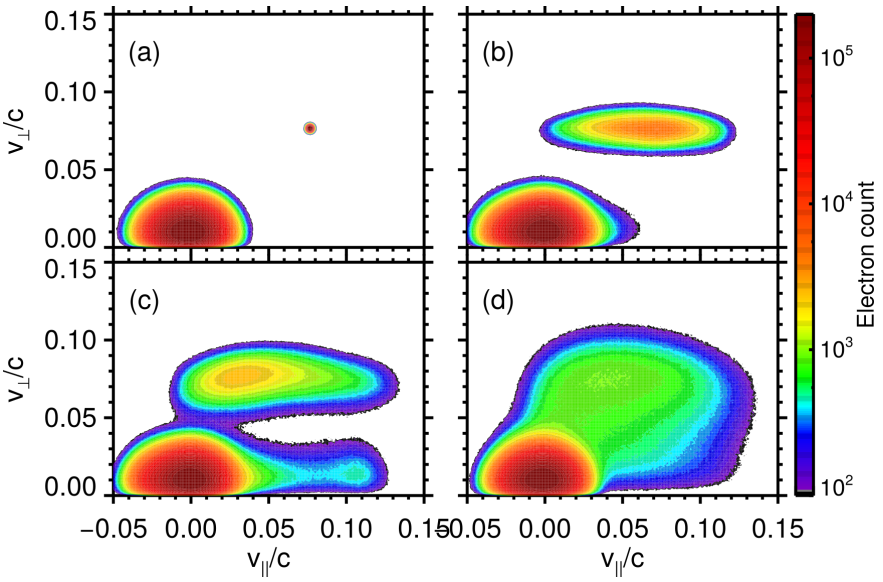


FIG. 6. The electron distribution in velocity space of $v_{\parallel}$ - $v_{\perp}$ at four selected time instants: (a) $t = 0$; (b) $t = 28\,\omega_{pe}^{-1}$; (c) $t = 35\,\omega_{pe}^{-1}$; (d) $t = 100\,\omega_{pe}^{-1}$. See the integral multimedia for an animation of the evolution of the electron distribution. (Multimedia view)

V. THE SUPPRESSION OF BEAM WHISTLER INSTABILITIES BY ELECTROSTATIC BEAM-MODE WAVE

The growth of whistler-mode waves through Landau resonance is limited by the growth of electrostatic beam-mode waves. The fast growing electrostatic waves saturate rapidly in a few plasma oscillations and deplete the beam free energy in the parallel direction through Landau resonance. Whistler waves saturate soon after the saturation of electrostatic beam-mode waves since there is little free energy left for the Landau resonant excitation of whistler waves. Such a competition between electrostatic and whistler instabilities depends on ω_{pe}/Ω_e, which characterizes the ratio between the linear growth rate of electrostatic instabilities and that of whistler instabilities. To test this idea and minimize the effect of cyclotron resonance, a field-aligned electron beam is used here while the rest of the setup is kept the same. Figure 7a shows the magnetic field energy of whistler waves with respect to time for a set of ω_{pe}/Ω_e values. Each of the color-coded lines corresponds to the colored spot in Figure 7b, in which the ratio of the saturated magnetic field energy to initial magnetic field energy is shown as a function of ω_{pe}/Ω_e. Under the special scenario of $\omega_{pe}/\Omega_e = 1$, whistler waves and electrostatic beam-mode waves saturate over the same time

scale and whistler waves saturate at a substantially larger amplitude compared to other cases. As ω_{pe}/Ω_e increases, the saturated whistler wave energy decreases and eventually is immersed in the noise level beyond $\omega_{pe}/\Omega_e = 7$. Linear theory predicts that Landau resonance between whistler waves and the electron beam does not occur beyond a critical value of $(\omega_{pe}/\Omega_e)_{critical} = 6.5$ for a cold beam in our parameter regime (see Appendix A for details). This inhibits the energy transfer between the beam electrons and whistler waves and results in a low signal to noise ratio in the high ω_{pe}/Ω_e regime. Below the critical value of $\omega_{pe}/\Omega_e = 6.5$, electrostatic instabilities limit the saturation energy level of whistler instabilities by extracting the free energy of the beam at a faster rate than the whistler instabilities as long as $\omega_{pe}/\Omega_e > 1$. It is also noted that there is a weak trend of decreasing signal to noise ratio beyond the critical value of $\omega_{pe}/\Omega_e = 6.5$. This may result from the fact that the theory prediction is for a cold beam while the distribution function is relaxed from the cold beam ring in the kinetic simulations and therefore it leads to a weak energy transfer between beam electrons and whistler waves even beyond the predicted critical value.

VI. SUMMARY AND DISCUSSION

Using a self-consistent Darwin particle-in-cell method, we study the excitation of electrostatic beam-mode and whistler waves in a beam-plasma system. The electrostatic beam-mode waves grow in magnitude rapidly and saturate in a few plasma oscillations, while the electron beam is slowed down and relaxed in the parallel direction. As the amplitude of electrostatic beam-mode waves approaches saturation, resonance with the tail of the background core electrons occurs and accelerates them parallel to the background magnetic field. Whistler waves grow in magnitude and saturate over the time scale of a few cyclotron periods. They are excited through Landau resonance and cyclotron resonance. In terms of wave propagation, electrostatic beam-mode waves are localized to the beam region, whereas whistler waves can leak out of the beam and transport energy away from the beam. Finally, the competition between electrostatic and whistler instabilities are tested for a field-aligned beam. Due to a faster depletion of the beam free energy by electrostatic beam-mode waves with increasing ω_{pe}/Ω_e, the saturation amplitude of whistler waves decreases. Beyond a critical ω_{pe}/Ω_e, Landau resonance does not occur for whistler waves and the saturation amplitude of whistler waves is immersed in the noise.

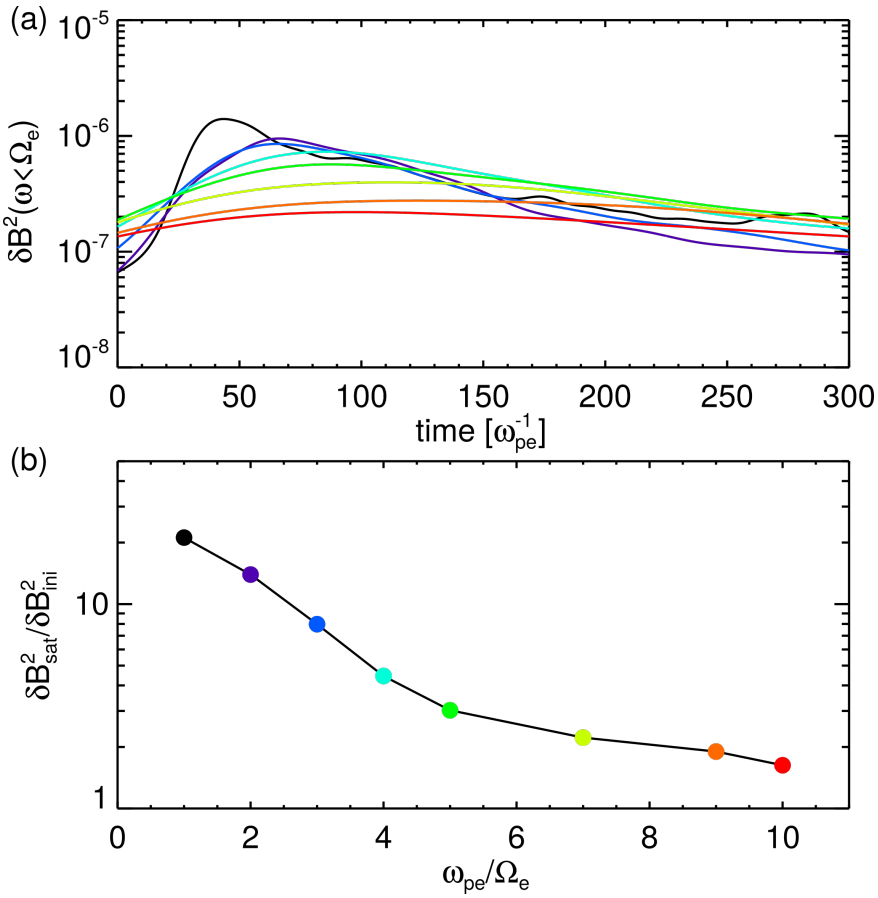


FIG. 7. (a) the evolution of magnetic field energy of whistler waves as a function of time. Starting from the black-blue line and going to the orange-red line, the corresponding values of ω_{pe}/Ω_e are $1, 2, 3, 4, 5, 7, 9, 10$. (b) Corresponding to each run in (a), the ratio of saturated energy to initial energy is shown as a function of ω_{pe}/Ω_e. Each colored spot corresponds to the line of the same color in panel (a).

There are still a number of differences between the kinetic simulation results and observations made with laboratory experiments. First, the PIC simulation is a relaxation of an initial beam whereas in the experiment, the beam electrons are continuously injected into the cold plasma. Second, the PIC simulation has the beam uniformly distributed along the parallel direction whereas in the experiment the beam source is fixed at a specific location along the parallel direction. In the experiment, it takes about 40 cyclotron periods or 200 plasma oscillations for the beam electrons to travel from the source location to the end of the experimental volume. In other words, the transit time of the beam electrons is

$\Delta t \approx 1257\,\omega_{pe}^{-1}$. In the PIC simulation with the ratio of beam density to total plasma density as $n_b/n_t = 0.125$, electrostatic beam-mode and whistler waves, respectively, saturate at $t = 30\,\omega_{pe}^{-1}$ and $t = 100\,\omega_{pe}^{-1}$. However, the saturation time of waves with the simulation value $n_b/n_t = 0.125$ should be properly scaled to the experimental value of $n_b/n_t = 0.001 \sim 0.005$. As a rough estimate, suppose that the saturation time of waves is inversely proportional to the linear growth rate of waves, i.e., $t_{sat} \propto 1/\gamma$, and that the linear growth rate of waves scales with the beam density[10,41] as $\gamma \propto (n_b/n_t)^{\frac{1}{3}}$ and hence $t_{sat} \propto (n_b/n_t)^{-\frac{1}{3}}$. Electrostatic beam-mode and whistler waves, respectively, are estimated to saturate at $t = 90 \sim 150\,\omega_{pe}^{-1}$ and $t = 300 \sim 500\,\omega_{pe}^{-1}$ in the experiment. Therefore it is expected that the electron distribution would be fully relaxed as in Figure 6d at the end of the experimental volume with a transit time of $\Delta t \approx 1257\,\omega_{pe}^{-1}$ in the experiment. The more realistic situation of the injection experiment driven by a beam source will be implemented in the PIC simulation in a future study.

Appendix A: A critical value of ω_{pe}/Ω_e for Landau resonance between whistler waves and beam electrons

It can be shown that[42] Landau resonance between whistler waves and beam electrons only occurs below some critical ω_{pe}/Ω_e. From the refractive index surface of whistler waves, there exists a minimum k_z for a given frequency

$$k_z^{\min} = \begin{cases} \dfrac{\omega_{pe}}{c}\dfrac{2\omega}{\Omega_e} & \omega < \dfrac{\Omega_e}{2} \\ \dfrac{\omega_{pe}}{c}\sqrt{\dfrac{\omega}{\Omega_e - \omega}} & \omega > \dfrac{\Omega_e}{2} \end{cases} \tag{A1}$$

Note that k_z takes the minimum value at the Gendrin angle for $\omega < \Omega_e/2$, while for $\omega > \Omega_e/2$, k_z takes the minimum value in the parallel direction. In order to have Landau resonance between beam electrons and whistler waves, the resonant wave number must exceed $k_z^{\min}$. That is

$$\frac{\omega}{v_z} > k_z^{\min} \tag{A2}$$

There exists a critical value of ω_{pe}/Ω_e, above which Landau resonance does not occur. This critical value is

$$\left(\frac{\omega_{pe}}{\Omega_e}\right)_{\text{critical}} = \begin{cases} \frac{c}{2v_z} & \omega < \frac{\Omega_e}{2} \\ \sqrt{\frac{\omega}{\Omega_e}\left(1-\frac{\omega}{\Omega_e}\right)}\frac{c}{v_z} & \omega > \frac{\Omega_e}{2} \end{cases} \tag{A3}$$

For typical parameters in the simulation, i.e., $v_z/c = 0.0766$ and $\omega/\Omega_e = 0.5$, the critical value of ω_{pe}/Ω_e is 6.5.

Appendix B: The equation of energy flux in the Darwin model

The energy flux equation in the Darwin model is

$$\nabla \cdot \mathbf{S} + \frac{\partial}{\partial t}\left[\frac{\mathbf{E}_L \cdot \mathbf{E}_L}{8\pi} + \frac{\mathbf{B}\cdot\mathbf{B}}{8\pi}\right] = -\mathbf{J}\cdot(\mathbf{E}_L + \mathbf{E}_T) \tag{B1}$$

where the Poynting flux takes the form of equation (4). $\mathbf{J}$ is the current density. Note that the energy of transverse electric field does not enter the field energy. The energy flux equation can be verified immediately by taking divergence of the Poynting flux in equation (4) and making use of the following set of equations

$$\nabla \times \mathbf{B} = \frac{4\pi}{c}\mathbf{J} + \frac{1}{c}\frac{\partial \mathbf{E}_L}{\partial t} \tag{B2}$$

$$\nabla \times \mathbf{E}_T = -\frac{1}{c}\frac{\partial \mathbf{B}}{\partial t} \tag{B3}$$

$$\nabla \cdot \mathbf{B} = 0 \tag{B4}$$

$$\nabla \cdot \mathbf{E}_T = 0 \tag{B5}$$

$$\nabla \times \mathbf{E}_L = 0 \tag{B6}$$

The transverse component of the displacement current is neglected in equation (B2) due to the Darwin approximation.

ACKNOWLEDGMENTS

We thank G. J. Morales for helpful discussions. We would also like to acknowledge high-performance computing support from Yellowstone (ark:/85065/d7wd3xhc) provided by NCAR's Computational and Information Systems Laboratory, sponsored by the National Science Foundation. The research was funded by the Department of Energy and the National

Science Foundation by grant DE-SC0010578, which was awarded to UCLA through the NSF/DOE Plasma Partnership program. The research was also funded by NASA grant NNX16AG21G.

REFERENCES

[1]R. L. Tokar, D. A. Gurnett, and W. C. Feldman, "Whistler mode turbulence generated by electron beams in earth's bow shock," Journal of Geophysical Research: Space Physics **89**, 105–114 (1984).

[2]E. Marsch, "Beam-driven electron acoustic waves upstream of the earth's bow shock," Journal of Geophysical Research: Space Physics **90**, 6327–6336 (1985).

[3]S. D. Bale, M. J. Reiner, J. L. Bougeret, M. L. Kaiser, S. Krucker, D. E. Larson, and R. P. Lin, "The source region of an interplanetary type II radio burst," Geophysical Research Letters **26**, 1573–1576 (1999).

[4]C. W. Carlson, J. P. McFadden, R. E. Ergun, M. Temerin, W. Peria, F. S. Mozer, D. M. Klumpar, E. G. Shelley, W. K. Peterson, E. Moebius, R. Elphic, R. Strangeway, C. Cattell, and R. Pfaff, "Fast observations in the downward auroral current region: Energetic upgoing electron beams, parallel potential drops, and ion heating," Geophysical Research Letters **25**, 2017–2020 (1998).

[5]J. E. Maggs, "Electrostatic noise generated by the auroral electron beam," Journal of Geophysical Research: Space Physics **83**, 3173–3188 (1978).

[6]V. Petrosian, "Impulsive solar x-ray bursts: bremsstrahlung radiation from a beam of electrons in the solar chromosphere and the total energy of solar flares," The Astrophysical Journal **186**, 291–304 (1973).

[7]J. Drake, M. Swisdak, C. Cattell, M. Shay, B. Rogers, and A. Zeiler, "Formation of electron holes and particle energization during magnetic reconnection," Science **299**, 873–877 (2003).

[8]P. L. Pritchett and F. V. Coroniti, "Three-dimensional collisionless magnetic reconnection in the presence of a guide field," Journal of Geophysical Research: Space Physics **109**, A01220 (2004).

[9]W. Li, D. Mourenas, A. V. Artemyev, J. Bortnik, R. M. Thorne, C. A. Kletzing, W. S. Kurth, G. B. Hospodarsky, G. D. Reeves, H. O. Funsten, and H. E. Spence, "Unravel-

ing the excitation mechanisms of highly oblique lower band chorus waves," Geophysical Research Letters **43**, 8867–8875 (2016), 2016GL070386.

[10]T. M. O'Neil, J. H. Winfrey, and J. H. Malmberg, "Nonlinear interaction of a small cold beam and a plasma," The Physics of Fluids **14**, 1204–1212 (1971), http://aip.scitation.org/doi/pdf/10.1063/1.1693587.

[11]K. W. Gentle and J. Lohr, "Experimental determination of the nonlinear interaction in a one dimensional beamplasma system," The Physics of Fluids **16**, 1464–1471 (1973), http://aip.scitation.org/doi/pdf/10.1063/1.1694543.

[12]J. E. Maggs, "coherent generation of VLF hiss," Journal of Geophysical Research **81**, 1707–1724 (1976).

[13]S. P. Gary and W. C. Feldman, "Solar wind heat flux regulation by the whistler instability," Journal of Geophysical Research **82**, 1087–1094 (1977).

[14]S. Y. Huang, H. S. Fu, Z. G. Yuan, A. Vaivads, Y. V. Khotyaintsev, A. Retino, M. Zhou, D. B. Graham, K. Fujimoto, F. Sahraoui, X. H. Deng, B. Ni, Y. Pang, S. Fu, D. D. Wang, and X. Zhou, "Two types of whistler waves in the hall reconnection region," Journal of Geophysical Research: Space Physics **121**, 6639–6646 (2016), 2016JA022650.

[15]D. L. Newman, M. V. Goldman, R. E. Ergun, and A. Mangeney, "Formation of double layers and electron holes in a current-driven space plasma," Phys. Rev. Lett. **87**, 255001 (2001).

[16]J. R. Winckler, "The application of artificial electron beams to magnetospheric research," Reviews of Geophysics **18**, 659–682 (1980).

[17]R. L. Stenzel, "Observation of beam-generated VLF hiss in a large laboratory plasma," Journal of Geophysical Research **82**, 4805–4814 (1977).

[18]C. Krafft, P. Thévenet, G. Matthieussent, B. Lundin, G. Belmont, B. Lembège, J. Solomon, J. Lavergnat, and T. Lehner, "Whistler wave emission by a modulated electron beam," Phys. Rev. Lett. **72**, 649–652 (1994).

[19]M. Starodubtsev and C. Krafft, "Resonant cyclotron emission of whistler waves by a modulated electron beam," Phys. Rev. Lett. **83**, 1335–1338 (1999).

[20]R. L. Morse and C. W. Nielson, "Numerical simulation of warm twobeam plasma," The Physics of Fluids **12**, 2418–2425 (1969), http://aip.scitation.org/doi/pdf/10.1063/1.1692361.

[21]Y. Omura and H. Matsumoto, "Competing processes of whistler and electrostatic instabilities in the magnetosphere," Journal of Geophysical Research: Space Physics **92**, 8649–8659 (1987).

[22]Y. Omura and H. Matsumoto, "Computer experiments on whistler and plasma wave emissions for spacelab-2 electron beam," Geophysical Research Letters **15**, 319–322 (1988).

[23]P. L. Pritchett, H. Karimabadi, and N. Omidi, "Generation mechanism of whistler waves produced by electron beam injection in space," Geophysical Research Letters **16**, 883–886 (1989).

[24]S. P. Gary, Y. Kazimura, H. Li, and J.-I. Sakai, "Simulations of electron/electron instabilities: Electromagnetic fluctuations," Physics of Plasmas **7**, 448–456 (2000), http://dx.doi.org/10.1063/1.873829.

[25]X. R. Fu, M. M. Cowee, K. Liu, S. P. Gary, and D. Winske, "Particle-in-cell simulations of velocity scattering of an anisotropic electron beam by electrostatic and electromagnetic instabilities," Physics of Plasmas **21**, 042108 (2014), http://dx.doi.org/10.1063/1.4870632.

[26]H. Che, M. L. Goldstein, P. H. Diamond, and R. Z. Sagdeev, "How electron two-stream instability drives cyclic langmuir collapse and continuous coherent emission," Proceedings of the National Academy of Sciences **114**, 1502–1507 (2017), http://www.pnas.org/content/114/7/1502.full.pdf.

[27]B. Van Compernolle, X. An, J. Bortnik, R. M. Thorne, P. Pribyl, and W. Gekelman, "Excitation of chirping whistler waves in a laboratory plasma," Phys. Rev. Lett. **114**, 245002 (2015); "Erratum: Excitation of chirping whistler waves in a laboratory plasma [phys. rev. lett. 114, 245002 (2015)]," Phys. Rev. Lett. **117**, 059901 (2016).

[28]X. An, B. Van Compernolle, J. Bortnik, R. M. Thorne, L. Chen, and W. Li, "Resonant excitation of whistler waves by a helical electron beam," Geophysical Research Letters **43**, 2413–2421 (2016), 2015GL067126.

[29]B. V. Compernolle, X. An, J. Bortnik, R. M. Thorne, P. Pribyl, and W. Gekelman, "Laboratory simulation of magnetospheric chorus wave generation," Plasma Physics and Controlled Fusion **59**, 014016 (2017).

[30]W. Gekelman, P. Pribyl, Z. Lucky, M. Drandell, D. Leneman, J. Maggs, S. Vincena, B. V. Compernolle, S. K. P. Tripathi, G. Morales, T. A. Carter, Y. Wang, and T. DeHaas, "The upgraded large plasma device, a machine for studying frontier basic plasma physics," Review of Scientific Instruments **87**, 025105 (2016), http://dx.doi.org/10.1063/1.4941079.

[31]V. K. Decyk, "UPIC: A framework for massively parallel particle-in-cell codes," Computer Physics Communications **177**, 95 – 97 (2007), proceedings of the Conference on Computational Physics 2006.

[32]`http://picksc.idre.ucla.edu/software/skeleton-code/`.

[33]R. S. Hughes, J. Wang, V. K. Decyk, and S. P. Gary, "Effects of variations in electron thermal velocity on the whistler anisotropy instability: Particle-in-cell simulations," Physics of Plasmas **23**, 042106 (2016), http://dx.doi.org/10.1063/1.4945748.

[34]D. Schriver, M. Ashour-Abdalla, F. V. Coroniti, J. N. LeBoeuf, V. Decyk, P. Travnicek, O. Santolk, D. Winningham, J. S. Pickett, M. L. Goldstein, and A. N. Fazakerley, "Generation of whistler mode emissions in the inner magnetosphere: An event study," Journal of Geophysical Research: Space Physics **115**, A00F17 (2010).

[35]X. An, C. Yue, J. Bortnik, V. Decyk, W. Li, and R. M. Thorne, "On the parameter dependence of the whistler anisotropy instability," Journal of Geophysical Research: Space Physics **122**, 2001–2009 (2017), 2017JA023895.

[36]J. Busnardo-Neto, P. Pritchett, A. Lin, and J. Dawson, "A self-consistent magnetostatic particle code for numerical simulation of plasmas," Journal of Computational Physics **23**, 300 – 312 (1977).

[37]J. Geary, T. Tajima, J.-N. Leboeuf, E. Zaidman, and J. Han, "Two- and three-dimensional magnetoinductive particle codes with guiding center electron motion," Computer Physics Communications **42**, 313 – 331 (1986).

[38]D. W. Hewett, "Elimination of electromagnetic radiation in plasma simulation: The darwin or magneto inductive approximation," in *Space Plasma Simulations: Proceedings of the Second International School for Space Simulations, Kapaa, Hawaii, February 4–15, 1985*, edited by M. Ashour-Abdalla and D. A. Dutton (Springer Netherlands, Dordrecht, 1985) pp. 29–40.

[39]A. Grossmann and J. Morlet, "Decomposition of hardy functions into square integrable wavelets of constant shape," SIAM Journal on Mathematical Analysis **15**, 723–736 (1984), http://dx.doi.org/10.1137/0515056.

[40]P. Goupillaud, A. Grossmann, and J. Morlet, "Cycle-octave and related transforms in seismic signal analysis," Geoexploration **23**, 85 – 102 (1984).

[41]T. F. Bell and O. Buneman, "Plasma instability in the whistler mode caused by a gyrating electron stream," Phys. Rev. **133**, A1300–A1302 (1964).

[42]M. Starodubtsev, C. Krafft, B. Lundin, and P. Thvenet, "Resonant cherenkov emission of whistlers by a modulated electron beam," Physics of Plasmas **6**, 2862–2869 (1999), http://dx.doi.org/10.1063/1.873244.